Applied Physics Letters

RESEARCH ARTICLE | MARCH 08 2024

High entropy alloy MoNbTaVW synthesized by metal-oxide reduction in a microwave plasma

Special Collection: Era of Entropy: Synthesis, Structure, Properties, and Applications of High-Entropy Materials

Bria Storr ; Shane A. Catledge

Appl. Phys. Lett. 124, 101905 (2024)
https://doi.org/10.1063/5.0192076

Applied Physics Letters ARTICLE pubs.aip.org/aip/apl

High entropy alloy MoNbTaVW synthesized by metal-oxide reduction in a microwave plasma

Cite as: Appl. Phys. Lett. **124**, 101905 (2024); doi: 10.1063/5.0192076
Submitted: 18 December 2023 · Accepted: 26 February 2024 ·
Published Online: 8 March 2024

Bria Storr and Shane A. Catledge[a]

AFFILIATIONS

Department of Physics, University of Alabama at Birmingham, Birmingham, Alabama 35294-1170, USA

Note: This paper is part of the APL Special Collection on Era of Entropy: Synthesis, Structure, Properties, and Applications of High Entropy Materials.
[a]**Author to whom correspondence should be addressed:** catledge@uab.edu

ABSTRACT

A unique approach was used to synthesize the high entropy alloy MoNbTaVW via reduction of metal-oxide precursors in a microwave plasma. The metal-oxides underwent ball milling and consolidation before plasma annealing at 1800 °C for 1 h with hydrogen as feedgas. X-ray diffraction, scanning electron microscopy/energy dispersive x-ray analysis, and Vickers hardness testing reveal characteristics of the high-entropy alloy. This includes a predominantly single-phase body-centered cubic structure, homogeneous distribution of all five metals, and 6.8 ± 0.9 GPa hardness, comparable with other reports for the same five-metal high entropy alloy configuration. Localized microwave plasma particle sintering is evident from the microstructure. These results highlight the promising potential of microwave plasma as a fast, economical, and flexible processing tool for high entropy alloys.

High entropy alloys (HEAs) have emerged as a captivating class of multi-component alloys characterized by their equimolar or near-equimolar composition and solid solution crystal structure. Specifically, refractory HEAs exhibit exceptional thermal stability, electrical conduction, and promising mechanical properties under extreme conditions.[1,2] The thermal stability, high melting point, remarkable mechanical strength, high toughness, oxidation resistance, and corrosion resistance make them a subject of active research and exploration. These properties are heavily dependent on the specific composition[3,4] and method of synthesis. The potential applications of HEAs include aerospace components, industrial machines (such as furnaces and cutting tools), and power generation systems, including components in gas turbines.[5,6]

Melting (e.g., vacuum arc melting or smelting) is the most widely used method for preparing refractory HEAs.[7,8] However, microstructural uniformity is a challenge due to component segregation, often requiring multiple melting steps. Powder metallurgy approaches using raw metal powders, followed by ball milling, and then spark plasma sintering can help mitigate these issues.[9,10] However, one must be very careful about powder contamination, which may negatively affect the mechanical properties of the alloys. These traditional synthesis methods present challenges ranging from cost and processing complexity to contamination, scalability issues, and inhomogeneity in the materials.[11–14]

To address the drawbacks associated with conventional HEA synthesis, this study explores a unique approach using a microwave (MW)-induced hydrogen plasma to reduce metal oxide precursors. A low-temperature molecular plasma is effective at driving electron-induced ionization and dissociation reactions to creative reactive radicals, expected to enhance kinetics and facilitate reduction of metal oxides in this process.[15–17] Unlike traditional reduction processes based on convective/radiant heating, microwave plasma excels in achieving high temperatures quickly and uniformly. This minimizes processing times and energy consumption,[18] due in large part to the efficient absorption of microwaves by the strongly dielectric metal oxide precursors and leads to volumetric heating. In addition, microwave sintering enhances densification of the material at lower process temperatures when compared to conventional sintering.[19,20] This can translate into shorter process times and less energy, with an improvement of the microstructure and mechanical properties.[21–23]

For high-temperature reaction experiments involving thermally activated chemical diffusion, the so-called "microwave effect" has been purported to enhance the process kinetics either by reducing the temperature or the time necessary to complete the reaction.[24] Possible mechanisms for enhanced kinetics and sinterability associated with the microwave effect have been attributed to the ponderomotive force

interaction,[25] to an electric field interaction with pores,[26] and to an anisothermal condition in multi-phasic systems.[27] Since bulk melting is not involved in the plasma annealing process, it also offers possibility of processing near-net-shape materials. The combination of microwave heating and sintering with the potential for enhanced reduction kinetics offered by the plasma may help overcome conventional limitations in producing HEAs and is promising for streamlining manufacturing processes.

Metal oxides of elements V, Nb, Ta, Mo, and W were chosen as precursors for the synthesis of the high entropy alloy MoNbTaVW. These precursor materials were sourced from Alfa Aesar: vanadium oxide (V_2O_5, 325 mesh, 99.2%), tantalum pentoxide (Ta_2O_5, <60 mesh, 99%), niobium oxide (Nb_2O_5, 99+%, 325 Mesh), molybdenum oxide (MoO_3, <325 mesh, 99.95%), and tungsten (WO_3, 325 mesh, 99%).

The appropriate amounts of the precursor powders were chosen via stoichiometry to produce a near equiatomic concentration corresponding to MoNbTaVW, as shown below:

$$MoO_3(s) + \frac{1}{2}Nb_2O_5(s) + \frac{1}{2}Ta_2O_5(s) + \frac{1}{2}V_2O_5(s) + WO_3(s) + \frac{27}{2}H_2(g) \rightarrow MoNbTaVW(s) + \frac{27}{2}H_2O(g).$$

The synthesis process started with the ball milling of the precursor metal oxides in a Spex 8000M high energy ball mill, utilizing a tungsten carbide (WC) vial. The milling procedure was divided into two segments, comprising 2 h of dry milling with WC balls followed by an additional 4 h of wet milling using zirconia (ZrO_2) balls. Post-milling, the precursor powders were passed through a 400-mesh sieve and then consolidated into a cohesive form using a 5 mm die via a uniaxial pressure of 500 MPa.

The consolidated pellet was placed on a molybdenum screw holder in a microwave plasma chamber (Wavemat, Inc., Plymouth, MI, USA; foe more details, see Ref. 28) and pumped to a base pressure of 150 mTorr prior to MW plasma annealing. Pure hydrogen feedgas (700 sccm H_2) was then added to the chamber and the plasma ignited by a 2.45 GHz magnetron. MW power and chamber pressure were increased to 0.60 kW and 40 Torr, respectively, resulting in the pellet temperature (measured by optical pyrometry) rapidly increasing at a rate of 80 °C per minute. The pellet temperature was held at 1000 °C for 30 min, followed by a further increase to 1800 °C for 1 h, made possible by increasing pressure and power to 140 Torr and 1.2 kW, respectively. At the end of this period, the MW power and flow of H_2 was turned off, allowing the sample to cool under vacuum.

Crystalline structure of the pre- and post-annealed pellets (after grinding into a powder) was analyzed using a Panalytical Empyrean x-ray diffractometer from the United Kingdom. A Cu-Kα anode ($\lambda = 1.541\,86$ Å) was used with power resulting from 45 kV and 40 mA settings. Each step of the diffraction pattern was recorded over a step duration of 16.32 s and increment of 0.0131° per step.

Microstructural details and elemental distribution were investigated utilizing an FEI Quanta FEG 650 SEM (Oregon, USA), with energy dispersive x-ray microanalysis (EDX). Image acquisition was performed at an accelerating voltage of 15 kV in order to discern microscale features of the MoNbTaVW HEA. Prior to EDX and hardness measurements, samples were polished using SiC papers followed by diamond-charged cloths down to 1 μm.

The hardness characteristics of the MoNbTaVW high entropy alloy were assessed using a Phase II+ 900-390A Vickers Hardness tester sourced from TEquipment (Long Branch, NJ, USA). To prepare the samples for hardness measurement, the annealed pellets were embedded in epoxy and ground using silicon carbide, progressing from 400 to 1500 grits. Subsequently, a polishing regimen with a diamond solution, ranging from 9 to 1 μm, was implemented using gold-label cloths (Allied High Tech, CA, USA). Three indents were collected for each load in the range from 10 to 500 gf (grams-force); each indent with a dwell time of 15 s.

The pellet, before and after plasma annealing, is shown in Fig. 1. The pellet color changes from yellow to gray and its diameter and height change from 5.00 and 1.45 mm to 2.74 and 1.18 mm, respectively, indicating transformation and loss of mass. In fact, the pellet mass reduced by 24.3% after the plasma annealing, as expected due to the reduction process and loss of oxygen. The post-annealed pellet density was measured by the Archimedes method to be 12.56 g/cm^3, while the density calculated using the XRD-calculated lattice parameter was 12.42 g/cm^3.

The microwave source effectively dissociates H_2 molecules into excited atomic hydrogen (observed from a strong Balmer line at 656.6 nm using optical emission spectroscopy). Hydrogen plasma efficiently reduces metal oxide bonds;[29] electrons are transferred to metal ions in the metal oxide, causing them to gain electrons and be reduced to their metallic state. Hydrogen plasma serves as a reducing agent in this process by providing a source of highly reactive hydrogen atoms and ions. The reactivity of atomic hydrogen, stemming from its radical nature and unfilled electronic orbital, facilitates the formation of new chemical bonds. These attribute renders atomic hydrogen an appealing choice as a reducing agent. It produces exhaustible water as a by-product akin to molecular hydrogen, while potentially offering broader applicability in reducing various metal oxides and demonstrating enhanced reaction rates.[30]

The XRD pattern of the pre- and post-plasma annealed material (in powder form) is shown in Fig. 2(a). The pre-annealed data (labeled as "Precursor") were obtained just after ball milling, but before consolidation into a pellet. The transformation from a multi-phase structure consisting of the five metal oxides to a predominantly single-phase body-centered cubic (BCC) structure after plasma annealing is evident and characteristic of the high entropy alloy. Weak shoulder peaks are

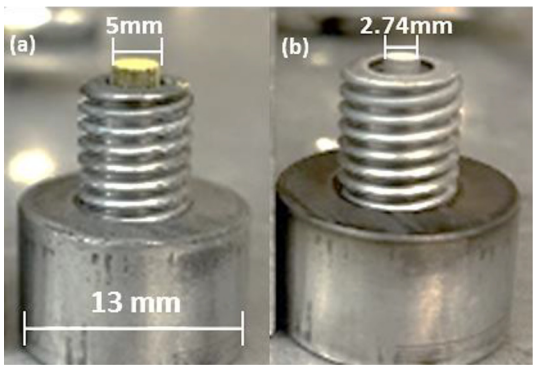

FIG. 1. Photographs of pellet on the Mo screw holder (a) before plasma annealing and (b) after plasma annealing.

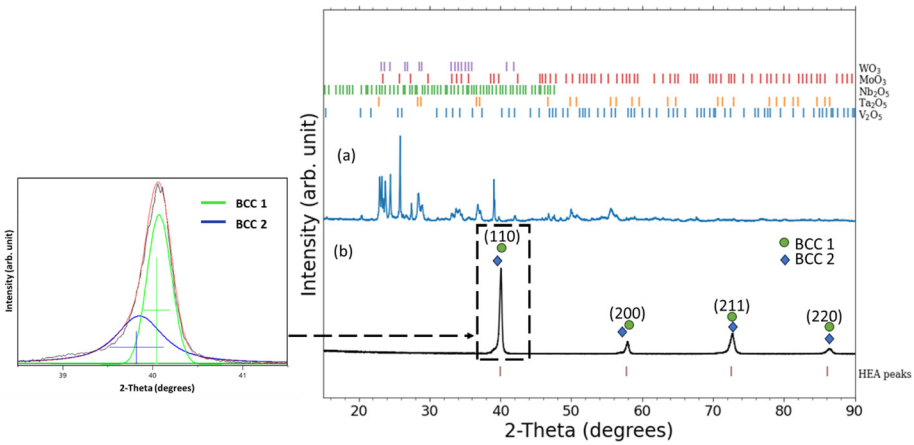

FIG. 2. (a) XRD powder patterns of pre- and post-plasma annealed material showing transformation to a predominantly single-phase BCC structure. The data labeled "Precursor" were obtained after ball milling but before plasma annealing and consists of the five metal oxides. The inset is two-theta region near the (110) peak showing fit to a primary and a minority BCC phase: BCC 1 (a = 3.1835 Å) and BCC 2 (a = 3.2004 Å).

found on the low-2θ side of each primary HEA peak suggesting a minority secondary BCC phase; see Fig. 2 inset for the region near the (110) diffraction peak. Rietveld refinement was performed after fitting all peaks in the post-plasma annealed sample. We observe no clear evidence (at least from a microstructural standpoint) of phase precipitation from the parent BCC phase. Although XRD shows very minor indication of what appears to be a second BCC phase, the microscopy data suggest this to be very close in composition to the primary phase, being perhaps a low- or medium-entropy variant (and unable to form contrast differences under microscopy). Rietveld analysis yields a fit to a ternary NbVW BCC phase (calculated lattice parameter of 3.2004 Å), but since metallographic analysis does not clearly bear this out, the shoulder peaks in XRD data indicate another very closely compositionally matched disordered phase.

Table I shows fitted lattice parameters for the primary BCC structure, along with values from other reports for the same five-element HEA configuration. The lattice parameter from this study is within 0.3% of the other reported values. The XRD data support the claim for effective reduction of the five metal oxides to yield a solid solution HEA from the plasma annealing process.

Scanning electron microscopy with energy-dispersive x-ray analysis (SEM/EDX) was used to demonstrate homogeneity of each of the five elements in the HEA sample. SEM on the pre-plasma annealed surface (i.e., the precursor powder after ball milling) is shown in Fig. 3(a), revealing a wide distribution of particle size from nanometer to micrometer. Figures 3(b) and 3(c) show SEM images of the post-plasma annealed pellet surface before and after polishing, respectively. The surface before polishing shows indication of particle sintering (evident as necking) with remaining porosity and micrometer-size spheroidal/oblong nodules. The sample was polished and etched with $HF:HNO_3:H_2O$ (1:1:8). The surface is relatively dense but still shows minor pitting inherent to the plasma process. As shown in Figs. 3(c) and 3(d), no secondary phase was observed, although minor porosity and scratches remain. The backscattered electrons (BSE) image in Fig. 3(d) also reveals the porosity and surface scratches but no clear indication of a second phase. The EDX elemental maps in Fig. 3(e) demonstrate uniform distribution and near equiatomic concentration for each of the five elements: V, Nb, Ta, Mo, and W. The results are consistent with the XRD data, as no residual metal oxides from the precursor were identified. Additionally, no contamination of oxygen and carbon was detected from SEM/EDX analysis. The uniform solid solution represents a characteristic feature of high entropy materials. The BSE and EDX images, together with the XRD data, indicate near equiatomic distribution of the five metals within the alloy microstructure. Such uniformity is important for HEA applications needed to achieve optimal mechanical and functional properties.

TABLE I. Reported lattice parameters compared to this work.

Method	Lattice parameter (Å)	Citation
MW-plasma	3.1856 (2)[a]	This work
Arc melting ref # 3	3.195	3
Arc melting ref # 11	3.185 (solidified) 3.187 (annealed)	11
Calculated	3.195	31

[a]With an uncertainty of ±0.0002.

Typically, HEAs are synthesized using arc melting. However, that approach is known to cause micro-segregation and possible dendritic structures.[32,33] This study shows that MW-plasma mitigates micro-segregation, as no bulk melting/re-solidification step is involved. This allows for microstructural homogeneity, as evidenced by SEM/EDX images in Fig. 3. Although XRD shows very minor indication of a second BCC phase, and the microscopy data suggest this phase is very close in composition to the primary phase, being perhaps a low- or medium-entropy variant. The MW plasma approach is, therefore, a viable alternative for synthesizing high entropy alloys with improved homogeneity.

Vickers hardness for the MoNbTaVW HEA polished pellet was measured at loads ranging from 10 to 500 gf, as shown in Fig. 4. An indentation size effect (ISE) is observed for this load range, with the hardness decreasing to 6.8 ± 0.9 GPa at the maximum load tested. Refractory high entropy alloys have been reported to have Vickers hardness ranging from 1.96 to 5.88 GPa.[34,35] For the same five-element HEA configuration used in this study, a hardness of 5.25 GPa (500 gf load, 30 s dwell time) was reported[32] for an HEA synthesized by the arc melting method. Computationally determined hardness values of 6.718 and 5.214 GPa have been reported for this alloy using the virtual crystal approximate method (VCA) and special quasi-random

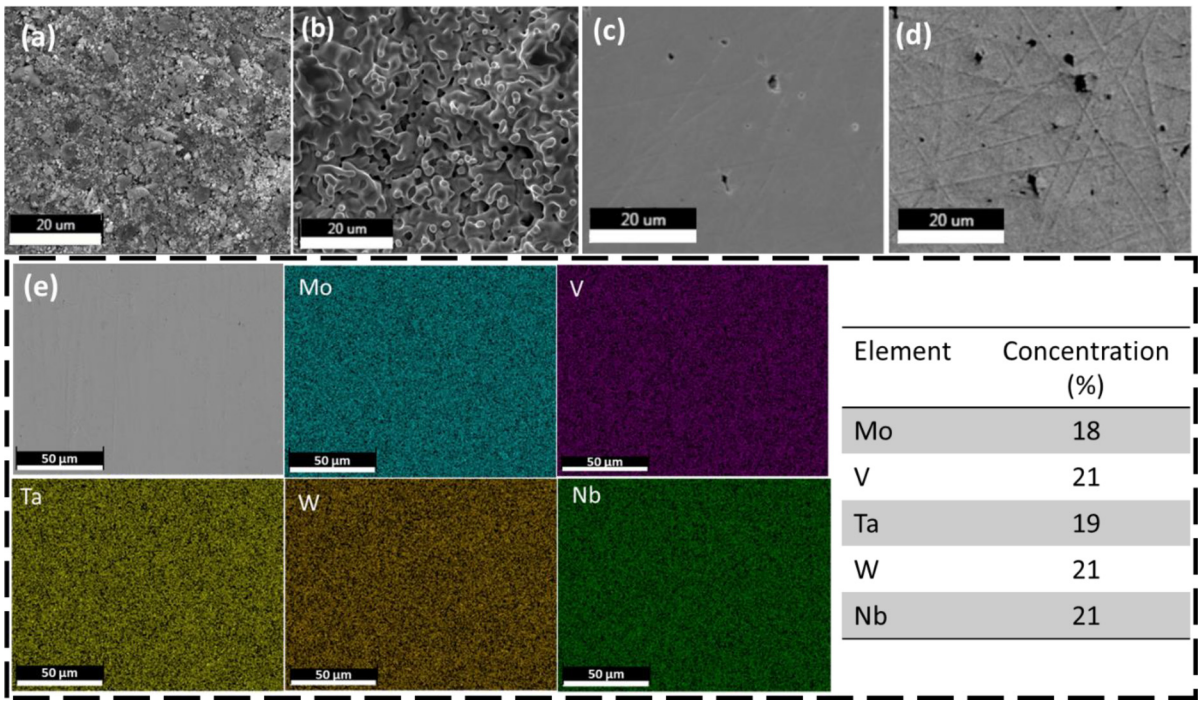

FIG. 3. SEM images of (a) pre-annealed pellet and (b) post-annealed pellet prior to polishing. Polished and etched portions of the HEA are presented as (c) secondary electron image and (d) backscattered electron image. (e) SEM and corresponding EDX elemental maps for each of the five elements in the HEA.

supercell method (SQS).[36] These computational results are comparable with the microwave plasma-annealed hardness measurement (6.8 GPa) obtained in this work.

The indentation size effect (ISE) is a phenomenon in which the mechanical properties of a material, such as hardness or elastic modulus, vary with the size or depth of the indentation created by an indenter. Understanding the underlying mechanisms is crucial for interpreting indentation data accurately and characterizing the mechanical behavior of materials at small scales.[37] At smaller indentation depths, the volume of material affected by the indentation decreases, leading to an accumulation of geometrically necessary dislocations (GNDs) that hinder further plastic deformation and contribute to increased hardness. These smaller indentations interact more with grain boundaries in polycrystalline materials, resulting in enhanced resistance to deformation and results in a stronger ISE.[38–40] Additionally, pileup and sink-in phenomena at different indentation depths influence the apparent hardness of the material.[41]

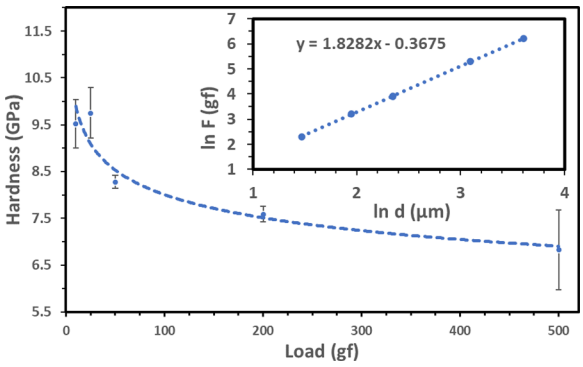

FIG. 4. Measured Vickers hardness for loads 10, 25, 50, 200, and 500 g revealing an indentation size effect (ISE). The ISE is confirmed by Meyers law as a linear plot of ln F vs ln d, where "F" is load and "d" is indent diagonal. The Meyers index was determined to be 1.83.

The ISE (manifested as a decrease in measured hardness with increasing load) can be described by Meyer's law,[42–45] as shown in the inset of Fig. 4. This is expressed as $lnF = lnA + nlnd$, where F is the load (gf), A is a hardness constant, and d is the mean value of the indentation diagonal (μm). A linear regression analysis was conducted on ln F vs ln d to obtain the slope that represents Meyer's index n. The index of 1.83 ± 0.01 determined from the linear regression is smaller than 2, further confirming the normal ISE behavior of the HEA. If n were less than 2, the material would have exhibited reverse-ISE, whereas if n were equal to 2, the hardness would follow conventional plasticity behavior.

Microwave plasma processing to produce MoNbTaVW HEA via metal oxide reduction represents a unique approach for synthesizing this class of materials. The oxide reduction to a predominantly single-phase BCC metallic structure with homogeneous distribution of each of the five metals is demonstrated by XRD and SEM/EDX. Localized microwave plasma particle sintering is evident from the microstructure and the measured Vickers hardness of 6.8 ± 0.9 GPa is comparable to that for same-element HEA configurations reported elsewhere. MW-plasma annealing demonstrates rapid heating rates, plasma-enhanced

reduction, and microwave sintering. It represents a promising alternative to conventional techniques for creating high entropy alloys that typically rely on melting/solidification routes.

This work was supported by the National Science Foundation (NSF) EPSCoR RII Track-1 Cooperative Agreement No. OIA-2148653 and by the National Science Foundation (NSF) Award No. DMR-2203112. Any opinions, findings, and conclusions or recommendations expressed in this material are those of the authors and do not necessarily reflect the views of the National Science Foundation.

AUTHOR DECLARATIONS

Conflict of Interest

The authors have no conflicts to disclose.

Author Contributions

Bria C. Storr: Data curation (supporting); Formal analysis (lead); Investigation (equal); Methodology (supporting); Writing – original draft (lead); Writing – review & editing (supporting). **Shane A. Catledge:** Conceptualization (lead); Funding acquisition (lead); Investigation (equal); Methodology (equal); Project administration (lead); Supervision (lead); Writing – review & editing (lead).

DATA AVAILABILITY

The data that support the findings of this study are available from the corresponding author upon reasonable request.

REFERENCES

[1]Y. Rao, C. Baruffi, A. De Luca, C. Leinenbach, and W. Curtin, "Theory-guided design of high-strength, high-melting point, ductile, low-density, single-phase BCC high entropy alloys," Acta Mater. **237**, 118132 (2022).
[2]K. Gao, Y. Chu, W. Zhou, Y. Tian, Y. Zhang, and Y. Li, "Phase inversion in a lightweight high Al content refractory high-entropy alloy," J. Mater. Sci. Technol. **150**, 124–137 (2023).
[3]C. Zhang, B. Yue, U. Bhandari, O. N. Starovoytov, Y. Yang, D. P. Young, J. Yan, F. Hong, and S. Yang, "*In situ* study on the compression deformation of MoNbTaVW high-entropy alloy," J. Alloys Compd. **871**, 159557 (2021).
[4]Y. Ma, Y. Zhang, Z. Zhang, L. Liu, and L. Sun, "Two novel Zr-rich refractory high-entropy alloys with excellent tensile mechanical properties," Intermetallics **157**, 107872 (2023).
[5]H. Huang, Y. Sun, P. Cao, Y. Wu, X. Liu, S. Jiang, H. Wang, and Z. Lu, "On cooling rates dependence of microstructure and mechanical properties of refractory high-entropy alloys HfTaTiZr and HfNbTiZr," Scr. Mater. **211**, 114506 (2022).
[6]W. Xiong, A. X. Guo, S. Zhan, C.-T. Liu, and S. C. Cao, "Refractory high-entropy alloys: A focused review of preparation methods and properties," J. Mater. Sci. Technol. **142**, 196–215 (2023).
[7]O. F. Dippo, N. Mesgarzadeh, T. J. Harrington, G. D. Schrader, and K. S. Vecchio, "Bulk high-entropy nitrides and carbonitrides," Sci. Rep. **10**(1), 21288 (2020).
[8]M. Li, Q. Chen, X. Cui, X. Peng, and G. Huang, "Evaluation of corrosion resistance of the single-phase light refractory high entropy alloy $TiCrVNb_{0.5}Al_{0.5}$ in chloride environment," J. Alloys Compd. **857**, 158278 (2021).
[9]Y. Long, X. Liang, K. Su, H. Peng, and X. Li, "A fine-grained NbMoTaWVCr refractory high-entropy alloy with ultra-high strength: Microstructural evolution and mechanical properties," J. Alloys Compd. **780**, 607–617 (2019).
[10]X. Yan, L. Constantin, Y. Lu, J. F. Silvain, M. Nastasi, and B. Cui, "$(Hf_{0.2}Zr_{0.2}Ta_{0.2}Nb_{0.2}Ti_{0.2})C$ high-entropy ceramics with low thermal conductivity," J. Am. Ceram. Soc. **101**(10), 4486–4491 (2018).
[11]O. N. Senkov, G. Wilks, J. Scott, and D. B. Miracle, "Mechanical properties of $Nb_{25}Mo_{25}Ta_{25}W_{25}$ and $V_{20}Nb_{20}Mo_{20}Ta_{20}W_{20}$ refractory high entropy alloys," Intermetallics **19**(5), 698–706 (2011).
[12]Q. Liu, G. Wang, X. Sui, Y. Xu, Y. Liu, and J. Yang, "Ultra-fine grain $Ti_xVNbMoTa$ refractory high-entropy alloys with superior mechanical properties fabricated by powder metallurgy," J. Alloys Compd. **865**, 158592 (2021).
[13]B. Kang, J. Lee, H. J. Ryu, and S. H. Hong, "Ultra-high strength WNbMoTaV high-entropy alloys with fine grain structure fabricated by powder metallurgical process," Mater. Sci. Eng. A **712**, 616–624 (2018).
[14]W. Huang, J. Hou, X. Wang, J. Qiao, and Y. Wu, "Excellent room-temperature tensile ductility in as-cast $Ti_{37}V_{15}Nb_{22}Hf_{23}W_3$ refractory high entropy alloys," Intermetallics **151**, 107735 (2022).
[15]A. Fridman, *Plasma Chemistry* (Cambridge University Press, 2008).
[16]W. H. Chiang, D. Mariotti, R. M. Sankaran, J. G. Eden, and K. Ostrikov, "Microplasmas for advanced materials and devices," Adv. Mater. **32**(18), 1905508 (2020).
[17]D. van den Bekerom, N. den Harder, T. Minea, N. Gatti, J. P. Linares, W. Bongers, R. van de Sanden, and G. van Rooij, "Non-equilibrium microwave plasma for efficient high temperature chemistry," J. Visualized Exp. **126**, e55066 (2017).
[18]K. D. Weltmann, J. F. Kolb, M. Holub, D. Uhrlandt, M. Šimek, K. Ostrikov, S. Hamaguchi, U. Cvelbar, M. Černák, B. Locke, A. Fridman, P. Favia, and K. Becker, "The future for plasma science and technology," Plasma Processes Polym. **16**(1), 1800118 (2019).
[19]J. Wang, J. Binner, B. Vaidhyanathan, N. Joomun, J. Kilner, G. Dimitrakis, and T. Cross, "Evidence for the microwave effect during hybrid sintering," J. Am. Ceram. Soc. **89**(6), 1977–1984 (2006).
[20]S. Charmond, C. P. Carry, and D. Bouvard, "Densification and microstructure evolution of Y-Tetragonal Zirconia Polycrystal powder during direct and hybrid microwave sintering in a single-mode cavity," J. Eur. Ceram. Soc. **30**(6), 1211–1221 (2010).
[21]Z. Xie, J. Yang, and Y. Huang, "Densification and grain growth of alumina by microwave processing," Mater. Lett. **37**(4–5), 215–220 (1998).
[22]D. Agrawal, "Microwave sintering of ceramics, composites and metallic materials, and melting of glasses," Trans. Indian Ceram. Soc. **65**(3), 129–144 (2006).
[23]A. Borrell and M. D. Salvador, "Advanced ceramic materials sintered by microwave technology," in *Sintering Technology - Method and Application* (InTechOpen, 2018), Vol. 10, pp. 3–24.
[24]J. H. Booske, R. F. Cooper, and S. A. Freeman, "Microwave enhanced reaction kinetics in ceramics," Mater. Res. Innovations **1**(2), 77–84 (1997).
[25]J. H. Booske, R. F. Cooper, S. A. Freeman, K. I. Rybakov, and V. E. Semenov, "Microwave ponderomotive forces in solid-state ionic plasmas," Phys. Plasmas **5**(5), 1664–1670 (1998).
[26]M. Willert-Porada, "A microstructural approach to the origin of 'microwave effects' in sintering of ceramics and composites," in *Microwaves: Theory and Application in Materials Processing IV, Ceramic Transactions* (American Ceramic Society, 1997), Vol. 80, pp. 153–156.
[27]R. D. Peelamedu, R. Roy, and D. Agrawal, "Anisothermal reaction synthesis of garnets, ferrites, and spinels in microwave field," Mater. Res. Bull. **36**(15), 2723–2739 (2001).
[28]B. Storr, L. Moore, K. Chakrabarty, Z. Mohammed, V. Rangari, C.-C. Chen, and S. A. Catledge, "Properties of high entropy borides synthesized via microwave-induced plasma," APL Mater. **10**(6), 061109 (2022).
[29]A. Rehman, R. W. van de Kruijs, W. T. van den Beld, J. M. Sturm, and M. Ackermann, "Chemical interaction of hydrogen radicals (H∗) with transition metal nitrides," J. Phys. Chem. C **127**(36), 17770–17780 (2023).
[30]H. J. Sceats, "On the reduction of metal oxides in non-equilibrium hydrogen plasmas," Ph.D. dissertation (Arthur Lakes Library, Colorado School of Mines, 2018).
[31]J. Byggmästar, K. Nordlund, and F. Djurabekova, "Modeling refractory high-entropy alloys with efficient machine-learned interatomic potentials: Defects and segregation," Phys. Rev. B **104**(10), 104101 (2021).
[32]O. Senkov, G. Wilks, D. Miracle, C. Chuang, and P. Liaw, "Refractory high-entropy alloys," Intermetallics **18**(9), 1758–1765 (2010).
[33]S. Kumar, A. Linda, Y. Shadangi, and V. Jindal, "Influence of micro-segregation on the microstructure, and microhardness of $MoNbTa_xTi_{(1-x)}W$ refractory high entropy alloys: Experimental and DFT approach," Intermetallics **164**, 108080 (2024).
[34]C. Zhang, H. Wang, X. Wang, Y. T. Tang, Q. Yu, C. Zhu, M. Xu, S. Zhao, R. Kou, and X. Wang, "Strong and ductile refractory high-entropy alloys with super formability," Acta Mater. **245**, 118602 (2023).

[35]T. Nagase, M. Todai, P. Wang, S.-H. Sun, and T. Nakano, "Design and development of (Ti, Zr, Hf)-Al based medium entropy alloys and high entropy alloys," Mater. Chem. Phys. **276**, 125409 (2022).
[36]Y. Hu, L. Bai, Y. Tong, D. Deng, X. Liang, J. Zhang, Y. Li, and Y. Chen, "First-principle calculation investigation of NbMoTaW based refractory high entropy alloys," J. Alloys Compd. **827**, 153963 (2020).
[37]Y. Huang, F. Zhang, K. Hwang, W. Nix, G. Pharr, and G. Feng, "A model of size effects in nano-indentation," J. Mech. Phys. Solids **54**(8), 1668–1686 (2006).
[38]L. Cui, C.-H. Yu, S. Jiang, X. Sun, R. L. Peng, J.-E. Lundgren, and J. Moverare, "A new approach for determining GND and SSD densities based on indentation size effect: An application to additive-manufactured Hastelloy X," J. Mater. Sci. Technol. **96**, 295–307 (2022).
[39]J. Engels, S. Gao, W. Amin, A. Biswas, A. Kostka, N. Vajragupta, and A. Hartmaier, "Indentation size effects in spherical nanoindentation analyzed by experiment and non-local crystal plasticity," Materialia **3**, 21–30 (2018).
[40]T. Bond, A. Badmos, R. Ahmed, J. Obayemi, A. Salifu, N. Rahbar, and W. Soboyejo, "Indentation size effects in aluminum and titanium alloys," Mater. Sci. Eng. A **839**, 142542 (2022).
[41]K. Durst, O. Franke, A. Böhner, and M. Göken, "Indentation size effect in Ni–Fe solid solutions," Acta Mater. **55**(20), 6825–6833 (2007).
[42]V. Matyunin, N. Abusaif, and A. Y. Marchenkov, "Analysis of the indentation size effect on the hardness measurements of materials," J. Phys.: Conf. Ser. **1399**, 044016 (2019).
[43]K. Sangwal, "On the reverse indentation size effect and microhardness measurement of solids," Mater. Chem. Phys. **63**(2), 145–152 (2000).
[44]U. Kölemen, "Analysis of ISE in microhardness measurements of bulk MgB_2 superconductors using different models," J. Alloys Compd. **425**(1–2), 429–435 (2006).
[45]J. Petrík, P. Blaško, Š. Markulík, M. Šolc, and P. Palfy, "The indentation size effect (ISE) of metals," Crystals **12**(6), 795 (2022).